CHEMISTRY OF MATERIALS

pubs.acs.org/cm

Article

Homologous Alkali Metal Copper Rare-Earth Chalcogenides $A_2Cu_{2n}Ln_4Q_{7+n}$ (n = 1, 2, 3)

Published as part of the Virtual Special Issue "John Goodenough at 100".

Craig C. Laing,[‖] Jiahong Shen,[‖] Michael A. Quintero, Benjamin E. Weiss, Yi Xia, Zhi Li, Jiangang He, Chris Wolverton, and Mercouri G. Kanatzidis*

Cite This: *Chem. Mater.* 2022, 34, 3409−3422

Read Online

ACCESS | Metrics & More | Article Recommendations | Supporting Information

ABSTRACT: Twenty-seven new members of the $A_2Cu_{2n}Ln_4Q_{7+n}$ (A = Cs, Rb; Ln = La−Nd, Sm, Gd−Yb; Q = S, Se) homologous series were synthesized in one of three structural types (indicated by n = 1, 2, 3). All the compounds contained 3D frameworks with alkali-metal-containing tunnels. For each increment in n, one Cu_2Q was added, which was incorporated into the framework as an edge-sharing tetrahedron by replacing a square planar chalcogenide site. High-throughput DFT calculations predicted many of the phases to be thermodynamically stable. These predictions were compared with the synthesis results for the phases formed in each composition space. In the syntheses, heavier lanthanides showed a preference to start forming the n = 3 $ACu_3Ln_2Q_5$, which is consistent with the predictions. $RbCuNd_2Se_4$ and $RbCuTb_2Se_4$ were found to be thermally stable under vacuum at temperatures up to 1000 °C. Optical measurements revealed band gaps of 1.55(5) and 1.62(5) eV for $CsCuCe_2Se_4$ and $RbCuTb_2Se_4$, respectively, and a work function of 4.83(5) eV for $CsCuPr_2Se_4$. Additionally, some n = 3 $ACu_3Ln_2Q_5$ compounds exhibit a negative phonon mode because of a copper atom coordination, which may distort to a trigonal planar geometry at sufficiently low temperatures. The dynamic instabilities and the predicted distortion in the copper tetrahedra for the n = 3 $ACu_3Ln_2Q_5$ compounds were found to have a linear relationship with the atomic number of the lanthanides and the electronegativity of the lanthanides. The $A_2Cu_{2n}Ln_4Q_{7+n}$ compounds can potentially find application as high-temperature thermoelectric materials and other semiconductors.

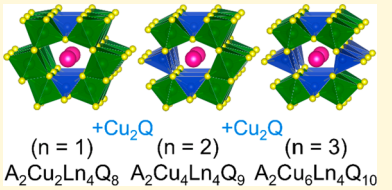

INTRODUCTION

Quaternary alkali metal rare-earth chalcogenide materials $A_aM_bLn_cQ_d$ (A = alkali metal, M = metal, Ln = lanthanide, Q = chalcogen) have large chemical phase spaces encompassing a variety of structures and compositions, which have not yet been fully explored. Many of the known structure types form either three-dimensional (3D) frameworks, such as $Rb_3Cu_5Nd_4Te_{10}$,[1] $CsTb_3STe_4$,[2] or $K_2Ag_3CeTe_4$[3] with tunnels of alkali metals, or two-dimensional (2D) structures, such as $CsGdZnSe_3$,[4] $RbTbZnTe_3$,[5] $RbLaGeS_4$,[6] or KCu_2EuTe_4[7] with alkali metal between the layers. The 3D structure types exhibit variations in the type of connections created between polyhedra to form the frameworks, in the shapes of the tunnels, and in the amounts of alkali metal atoms in the tunnels. The 2D structure types exhibit variations in connections between polyhedra to form the layers and how flat or corrugated the layers are. These materials have been studied for properties including superconductivity, charge-density waves,[8] thermoelectrics, and magnetism.[9] Mitchell and Ibers further discussed many of the known structure types for rare-earth transition metal chalcogenides in a review.[9] The present work examines new sulfide and selenide materials that crystallize with the composition $ACuLn_2Q_4$,[10−18] $A_2Cu_4Ln_4Q_9$,[13−15] or $ACu_3Ln_2Q_5$[14−16,19−22] (A = K, Rb, Cs; Ln = La−Sm, Gd−Yb; Q = S, Se) as 3D tunnel structure types and defines the homologous relationship[23] between these three structure types.

Herein, we report the synthesis and structure of 27 compounds crystallized in the homologous series $A_2Cu_{2n}Ln_4Q_{7+n}$ (n = 1, 2, or 3) from the compositional space A/Cu/Ln/Q (A = Cs, Rb; Ln = La−Sm, Gd−Yb; Q = S, Se). This three-member homologous series incorporates one equivalent of Cu_2Q for each increment in n by adding copper tetrahedra to the 3D framework at the square planar chalcogenide site. For select members of the series, the thermal, optical, and electronic properties were characterized using differential thermal analysis (DTA), UV−vis spectroscopy, photoemission yield spectroscopy in air (PYSA), and first-principles density functional theory (DFT) calculations. It was found that these materials are thermally stable in vacuum at temperatures of up to 1000 °C. $CsCuCe_2Se_4$ and

Received: January 25, 2022
Revised: March 1, 2022
Published: March 21, 2022

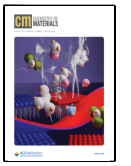

Table 1. Crystallographic and Structure Refinement Data of $Rb_2Cu_{2n}Dy_4S_{7+n}$ Compounds[a]

empirical formula	$RbCuDy_2S_4$ (n = 1)	$Rb_2Cu_4Dy_4S_9$ (n = 2)	$RbCu_3Dy_2S_5$ (n = 3)
formula weight	1204.50	1363.64	1522.78
crystal system	orthorhombic	monoclinic	orthorhombic
space group	*Cmcm*	*C*2/*m*	*Cmcm*
unit cell dimensions	a = 3.9791(8) Å	a = 13.867(3) Å	a = 3.9518(8) Å
	b = 13.621(3) Å	b = 3.9659(8) Å	b = 13.951(3) Å
	c = 13.764(3) Å	c = 15.938(3) Å	c = 16.473(3) Å
	$\alpha = \beta = \gamma$ = 90°	$\alpha = \gamma$ = 90°	$\alpha = \beta = \gamma$ = 90°
		β = 109.23(3)°	
volume	746.0(3) Å^3	827.6(3) Å^3	908.2(3) Å^3
density (calculated)	5.362 g/cm^3	5.472 g/cm^3	5.569 g/cm^3
independent reflections	608	4958	1388
	[R_{int} = 0.0380]	[R_{int} = 0.0246]	[R_{int} = 0.0196]
completeness to θ = 25.242°	98.5%	99.7%	98.8%
goodness-of-fit	1.060	1.038	1.018
final R indices [$I > 2\sigma(I)$]	R_{obs} = 0.0452, wR_{obs} = 0.1019	R_{obs} = 0.0515, wR_{obs} = 0.1217	R_{obs} = 0.0204, wR_{obs} = 0.0464
R indices [all data]	R_{all} = 0.0660, wR_{all} = 0.1132	R_{all} = 0.0740, wR_{all} = 0.1334	R_{all} = 0.0299, wR_{all} = 0.0481
largest diffraction peak and hole	1.802 and −1.481 e·Å^{-3}	4.362 and −2.367 e·Å^{-3}	1.934 and −2.304 e·Å^{-3}

[a] $R = \sum||F_o| - |F_c||/\sum|F_o|$, $wR = \{\sum[w(|F_o|^2 - |F_c|^2)^2]/\sum[w(|F_o|^4)]\}^{1/2}$, and $w = 1/[\sigma^2(F_o^2) + (P)^2 + P]$, where $P = (F_o^2 + 2F_c^2)/3$.

$RbCuTb_2Se_4$ were found to have band gaps of 1.55(5) and 1.62(5) eV, respectively. Additionally, some of the n = 3 $ACu_3Ln_2Q_5$ members exhibited dynamic instability, as indicated by the negative phonon modes observed in phonon-dispersion calculations.

EXPERIMENTAL METHODS

Reagents. Cs (99.5%, Alfa Aesar), Rb (99.5% Alfa Aesar), S (99.99%, 5 N Plus Inc.), Se (99.99%, American Elements), CsCl (99.9%, Alfa Aesar), RbCl (99.8%, MilliporeSigma), and RbBr (99.8%, MilliporeSigma) were used as purchased without additional purification. Cu (99.7%, MilliporeSigma) powder was activated by washing with 10% by weight HCl, followed by a deionized water rinse and drying with isopropanol in a vacuum filter. It was then stored in a glovebox. Lanthanide chunks were used by first removing the tarnished surface with a diamond file and then collecting fresh shavings from the pristine metallic surface.

A_2Q Synthesis (A = Cs, Rb; Q = S, Se). Batches of 15 g of A_2Q (A = Cs, Rb; Q = S, Se) were prepared using stoichiometric reactions of the two respective elements in liquid ammonia NH_3.[24,25] Opened glass ampules containing elemental Cs or Rb were slightly heated (~30 and ~40 °C, respectively) on a hot plate and pipetted into a 250 mL three-neck round-bottom flask with a Teflon valve containing a magnetic stir bar enclosed in glass in a nitrogen glovebox. The airtight flask was then closed and transferred to a Schlenk line. The line was then purged with nitrogen, and 150 mL of ammonia gas condensed into the flask at −78 °C with a dry ice/acetone bath and was allowed to dissolve the alkali metal for approximately 1 h, forming a dark blue solution. The respective chalcogenide was then added to the mixture and stirred for several hours. The ammonia was allowed to evaporate under nitrogen flow by allowing the dry ice/acetone bath to warm to room temperature. The air-sensitive white/pale yellow product was then dried overnight under vacuum and stored in a glovebox.

$A_2Cu_{2n}Ln_4Q_{7+n}$ Synthesis. $A_2Cu_{2n}Ln_4Q_{7+n}$ compounds were synthesized for almost all the compounds reported here using a stoichiometric combination of A_2Q (A = Cs, Rb; Q = S, Se), Cu, Ln, and either S or Se in a 1:10 molar ratio with AX (CsCl, RbCl, or RbBr) with the matching alkali metal as a salt flux. For example, for $CsCuNd_2S_4$, CsCl (1.246 g, 7.401 mmol), Cs_2S (0.110 g, 0.369 mmol), Cu (0.047 g, 0.740 mmol), Nd (0.214 g, 1.48 mmol), and S (0.083 g, 2.59 mmol) were combined in a 20:1:2:4:7 molar ratio of CsCl:Cs_2S:Cu:Nd:S, yielding a molar ratio of 10 equivalents of CsCl to 1 equivalent of $CsCuNd_2S_4$. A full list of the reaction conditions is provided in Table S1. Because of the high reactivity of activated copper with sulfur powder, the reaction is sufficiently exothermic to vaporize sulfur when ground in a mortar and pestle. Hence, copper and the sulfur powder were allowed to react in a mortar and pestle in the glovebox until the mixture turned black before homogenizing with the fresh lanthanide shavings, A_2Q, and AX.[26] The material was then charged in a graphite crucible with an outer diameter of 12.7 mm and depth of ~32 mm, and a graphite lid was placed on top. The crucible was then placed in a fused silica tube with outer and inner diameters of 15 and 13 mm, respectively, and three layers of carbon coating. It was then transferred to a vacuum line, evacuated to 2.8×10^{-3} mbar, and then flame-sealed with a torch. The sealed tube was then placed inside a mullite tube in a one-zone tube furnace packed with insulation wool. To suppress volatilization during the reaction, the tube was positioned such that the crucible with the reagents was adjacent to the thermocouple and the top of the fused silica tube was just below the center of the tube furnace, which is the hottest region of the furnace. For $CsCuNd_2S_4$, the furnace was heated to 800 °C for 16 h and held at this temperature for 72 h. The furnace was then switched off and allowed to cool to room temperature. A full list of the heating profiles is provided in Table S1. The product was washed by sonication in methanol, followed by decanting until no more white salt could be removed. The remaining product was then dried by passing nitrogen over it. The sulfides were all in the form of red needles, except $CsCuPr_2S_4$, which was in the form of orange needles, while all the selenides were in the form of black needles. The product was then mechanically separated for characterization from various side products, including CuQ binaries, LnQ binaries, $ALnQ_2$, $CuLnQ_2$, $A_3Er_7Q_{12}$, and some unidentified side products. The yield for each reaction is provided in Table S1.

Single Crystal X-ray Diffraction. Intensity data was collected from suitable needle-shaped single crystals mounted on a glass fiber with super glue from a STOE IPDS 2, a STOE IPDS 2T, or a STOE StadiVari diffractometer at 293 K. Intensity data was also collected for a suitable crystal of $CsCu_3Tb_2S_5$ on a STOE StadiVari diffractometer at both 6 and 480 K. The STOE IPDS 2 and STOE IPDS 2T diffractometers were equipped with a Mo K_α (λ = 0.71073 Å) sealed X-ray source with X-ray fiber optics and an image plate detector. The STOE StadiVari diffractometer was equipped with an AXO Auxilia Microfocus Ag Kα (λ = 0.56083 Å) sealed X-ray source and a Dectris Pilatus3 R CdTe 300 K hybrid photon-counting detector. Data reduction was performed using the STOE X-Area version 1.90 software package. A numerical absorption correction was applied using STOE X-Red version 1.65.2 and STOE X-Shape version 2.21, followed by scaling and outlier rejection with STOE LANA version 1.83.8.[27] The structure was solved using the ShelXT intrinsic phasing solution method[28] and refined by applying the ShelXL full matrix least-squares minimization on the F^2 method.[29] Olex2[30] was used as

https://doi.org/10.1021/acs.chemmater.2c00223
Chem. Mater. 2022, 34, 3409−3422

Table 2. Crystallographic and Structure Refinement Data of n = 1 $ACuPr_2Q_4$ Compounds[a]

empirical formula	$RbCuPr_2S_4$	$RbCuPr_2Se_4$	$CsCuPr_2S_4$	$CsCuPr_2Se_4$
formula weight	1118.14	1493.34	1213.02	1588.22
crystal system	orthorhombic	orthorhombic	orthorhombic	orthorhombic
space group	*Cmcm*	*Cmcm*	*Cmcm*	*Cmcm*
unit cell dimensions	a = 4.1034(8) Å	a = 4.2367(8) Å	a = 4.1283(8) Å	a = 4.2642(9) Å
	b = 14.032(3) Å	b = 14.505(3) Å	b = 14.331(3) Å	b = 14.823(3) Å
	c = 14.031(3) Å	c = 14.593(3) Å	c = 14.120(3) Å	c = 14.656(3) Å
	$\alpha = \beta = \gamma$ = 90°	$\alpha = \beta = \gamma$ = 90°	$\alpha = \beta = \gamma$ = 90°	$\alpha = \beta = \gamma$ = 90°
volume	807.9(3) Å^3	896.8(3) Å^3	835.4(3) Å^3	926.4(3) Å^3
density (calculated)	4.597 g/cm^3	5.530 g/cm^3	4.822 g/cm^3	5.694 g/cm^3
independent reflections	725	979	1392	806
	[R_{int} = 0.0491]	[R_{int} = 0.0185]	[R_{int} = 0.0328]	[R_{int} = 0.0305]
completeness to θ = 25.242°	100%	98.5%	99.6%	99.8%
goodness-of-fit	1.156	1.227	1.043	1.197
final R indices [$I > 2\sigma(I)$]	R_{obs} = 0.0381, wR_{obs} = 0.0762	R_{obs} = 0.0250, wR_{obs} = 0.0641	R_{obs} = 0.0352, wR_{obs} = 0.0776	R_{obs} = 0.0338, wR_{obs} = 0.0782
R indices [all data]	R_{all} = 0.0622, wR_{all} = 0.0847	R_{all} = 0.0274, wR_{all} = 0.0651	R_{all} = 0.0568, wR_{all} = 0.0866	R_{all} = 0.0507, wR_{all} = 0.0906
largest diffraction peak and hole	1.924 and −1.784 e·Å^{-3}	1.577 and −2.519 e·Å^{-3}	1.942 and −2.644 e·Å^{-3}	2.147 and −2.260 e·Å^{-3}

[a] $R = \sum||F_o| - |F_c||/\sum|F_o|$, $wR = \{\sum[w(|F_o|^2 - |F_c|^2)^2]/\sum[w(|F_o|^4)]\}^{1/2}$, and $w = 1/[\sigma^2(F_o^2) + (P)^2 + P]$, where $P = (F_o^2 + 2F_c^2)/3$.

Table 3. Crystallographic and Structure Refinement Data of n = 3 $ACu_3Tm_2Q_5$ Compounds[a]

empirical formula	$RbCu_3Tm_2S_5$	$RbCu_3Tm_2Se_5$	$CsCu_3Tm_2S_5$
formula weight	1548.50	2017.50	1643.38
crystal system	orthorhombic	orthorhombic	orthorhombic
space group	*Cmcm*	*Cmcm*	*Cmcm*
unit cell dimensions	a = 3.9266(8) Å	a = 4.0829(8) Å	a = 3.9352(8) Å
	b = 13.916(3) Å	b = 14.496(3) Å	b = 14.062(3) Å
	c = 16.323(3) Å	c = 16.917(3) Å	c = 16.576(3) Å
	$\alpha = \beta = \gamma$ = 90°	$\alpha = \beta = \gamma$ = 90°	$\alpha = \beta = \gamma$ = 90°
volume	891.9(3) Å^3	1001.2(3) Å^3	917.3(3) Å^3
density (calculated)	5.766 g/cm^3	6.692 g/cm^3	5.950 g/cm^3
independent reflections	1196	887	871
	[R_{int} = 0.0564]	[R_{int} = 0.0218]	[R_{int} = 0.0299]
completeness to θ = 25.242°	99.8%	99.8%	99.7%
goodness-of-fit	0.947	1.222	1.158
final R indices [$I > 2\sigma(I)$]	R_{obs} = 0.0407, wR_{obs} = 0.0828	R_{obs} = 0.0287, wR_{obs} = 0.0643	R_{obs} = 0.0355, wR_{obs} = 0.0627
R indices [all data]	R_{all} = 0.0637, wR_{all} = 0.0885	R_{all} = 0.0348, wR_{all} = 0.0662	R_{all} = 0.0538, wR_{all} = 0.0681
largest diff. peak and hole	2.310 and −3.053 e·Å^{-3}	2.165 and −4.124 e·Å^{-3}	1.904 and −2.210 e·Å^{-3}

[a] $R = \sum||F_o| - |F_c||/\sum|F_o|$, $wR = \{\sum[w(|F_o|^2 - |F_c|^2)^2]/\sum[w(|F_o|^4)]\}^{1/2}$, and $w = 1/[\sigma^2(F_o^2) + (P)^2 + P]$, where $P = (F_o^2 + 2F_c^2)/3$.

the graphical interface. The crystallographic information can be found in Tables 1−3 and Tables S2−S93.

Photoemission Yield Spectroscopy in Air (PYSA). A Riken-Keiki AC-2 instrument was used to perform PYSA. The sample was scanned using a tunable monochromatic ultraviolet light (UV, 4.2−6.2 eV) in dry air. Photoelectrons were measured at each excitation energy and generated only when the photon energy is higher than the work function, which is equal to the maximum energy of the valence band with respect to the vacuum energy. The work function was determined from the linear onset of the PYSA spectra.

High-Throughput Density Functional Theory (HT-DFT) Calculations. All DFT[31,32] calculations were performed using the Vienna Ab initio Simulation Package (VASP)[33,34] along with the projector augmented wave[35] pseudopotential. The Perdew−Burke−Ernzerhof[36,37] version of the generalized gradient approximation was used as the exchange-correlation functional. High-throughput calculations and convex hull construction were carried out within the OQMD framework (oqmd.org, currently containing more than 1 000 000 different compounds).[38,39] In this work, the stability (i.e., convex hull distance) was defined to be positive for unstable compounds, indicating the difference between the formation energy of the unstable phase and the hull energy at this composition. For the stable phase P, however, the stability was defined as the difference between the energy of the previous convex hull (i.e., the convex hull without P) at this composition and the formation energy of P, yielding a negative value, which indicates the degree of stability (i.e., energy driven force of forming the compound).

Electronic Band Structure, Phonon Dispersion, and Thermoelectric Property Calculations. DFT calculations were carried out to obtain the electronic structure, phonon dispersion, and thermoelectric properties of the $A_2Cu_{2n}Ln_4Q_{7+n}$ (n = 1, 2, or 3) compounds. A Γ-centered k-mesh with at least 8000 k-points per reciprocal atom was used to sample the Brillouin zone of primitive cell compounds. A plane-wave basis set with a cutoff energy of 520 eV was used, and all the structures were fully relaxed until the total energy converged to 10^{-8} eV. The total forces on each atom were less than 0.01 eV/Å. Phonon calculations were performed with 2 × 2 × 2 conventional cells using the PHONOPY package.[40] Anharmonic effects were taken into account to calculate the phonon dispersions at finite temperatures for the selected compounds with unstable phonon modes at T = 0 K. Renormalized phonon frequencies were obtained by solving the self-consistent phonon equation at a given temperature, as implemented by Xia et al.[41] The anharmonic force constants including both cubic and quartic terms were constructed using compressive sensing lattice dynamics (CSLD).[42−44] The lattice thermal conductivity was calculated by solving the phonon Boltzmann transport equation as implemented by ShengBTE.[45] The semiclassical Boltzmann transport theory was implemented in the BoltzTraP[46]

https://doi.org/10.1021/acs.chemmater.2c00223
Chem. Mater. 2022, 34, 3409−3422

package and used to calculate the electrical transport properties, Seebeck coefficient, and carrier thermal conductivity under the relaxation time approximation. The calculation of the electron−phonon coupling matrix elements g in eq 4.48 of the work by Grimvall is the most computationally expensive step in determining the carrier relaxation time.[47] In this study, we used the efficient formalism implemented in code in AMSET by Ganose et al.[48] to calculate the carrier relaxation time using multiple reasonable approximations. We considered acoustic deformation potential (ADP) scattering, polar optical phonon (POP) scattering, and ionized impurity (IMP) scattering as these are typically the dominant scattering mechanisms in thermoelectrics. The total relaxation time, $\tau^{-1} = \tau_{ADP}^{-1} + \tau_{POP}^{-1} + \tau_{IMP}^{-1}$, is determined according to Mathiessen's rule. The construction of g requires knowledge of several intrinsic material parameters such as the elastic constant tensor $\boldsymbol{C}$, dielectric constant tensor $\boldsymbol{\varepsilon}$, polar phonon frequency ω, and deformation potential constant tensor $\boldsymbol{d}$. The former three were directly generated in VASP while the last was fitted by constructing a series of deformed structures with lattice constants of $0.99l_0$, $0.995l_0$, l_0, $1.005l_0$, and $1.1l_0$ along the three Cartesian axes. The thermoelectric figure of merit ZT was calculated as $S^2\sigma T/(k_e + k_l)$, where is S the Seebeck coefficient, σ the electrical conductivity, T the temperature, and k_e and k_l are electronic and lattice thermal conductivities, respectively.

RESULTS AND DISCUSSION

Structure and Homologous Relationship. The 27 compounds reported here are part of a three-member homologous relationship, defined as $A_2Cu_{2n}Ln_4Q_{7+n}$ (n = 1, 2, 3), as shown in Figure 1. All of them are 3D framework

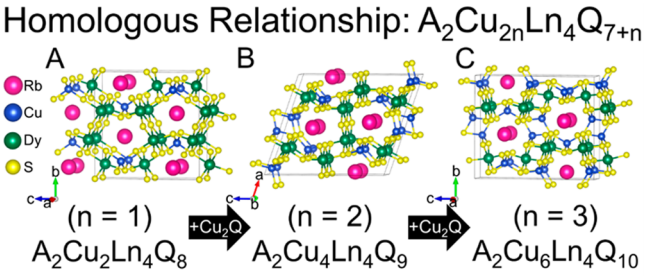

Figure 1. Three-member homologous series of the general formula $A_2Cu_{2n}Ln_4Q_{7+n}$ showing the evolving structures of (A) $RbCuDy_2S_4$ (n = 1), (B) $Rb_2Cu_4Dy_4S_9$ (n = 2), and (C) $RbCu_3Dy_2S_5$ (n = 3). Each additional Cu_2Q incorporated into the framework replaces a square planar chalcogenide site with two edge-sharing copper chalcogenide tetrahedra.

materials with alkali metal-containing tunnels. Each increment in n corresponds to adding one equivalent of Cu_2Q to the composition, which changes the structure of the 3D framework. The $ACuLn_2Q_4$ compounds reported here crystallize in the n = 1 ($A_2Cu_2Ln_4Q_8$) $KcuGd_2S_4$ structure type[12] with the *Cmcm* space group shown in Figure 1A. A close-up of the tunnel is shown in Figure 2A, and the alkali metal coordination environment is shown in Figure 3A. The 3D anionic framework is composed of CuQ_4 tetrahedra and LnQ_6 octahedra, which form corrugated layers. The individual corrugated layers are composed of three polyhedra (LnQ_6−CuQ_4−LnQ_6), which repeat along the [001] direction and extend across the (010) plane with edge-sharing connectivity. The tunnels propagate in the [100] direction and are one alkali-metal wide, filled with 8-coordinate AQ_8 polyhedra (Figure 3A). The inner wall of the tunnel is composed of eight polyhedra from two successive layers. One layer contributes a three-polyhedra unit (LnQ_6−CuQ_4−LnQ_6), while the other

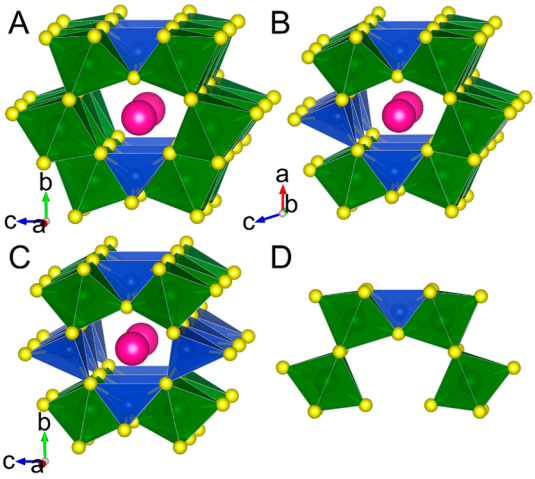

Figure 2. Eight polyhedra forming the tunnel in (A) $RbCuDy_2S_4$ (n = 1), (B) $Rb_2Cu_4Dy_4S_9$ (n = 2), and (C) $RbCu_3Dy_2S_5$ (n = 3). (D) 5-Polyhedra unit containing the three polyhedra that constitute these framework structures.

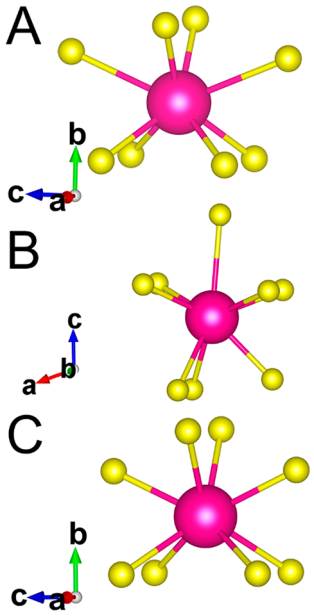

Figure 3. Coordination environment of the alkali metal in (A) $RbCuDy_2S_4$ (n = 1), (B) $Rb_2Cu_4Dy_4S_9$ (n = 2), and (C) $RbCu_3Dy_2S_5$ (n = 3).

contributes five polyhedra, as shown in Figure 2D. The five polyhedra have a repeating (LnQ_6−CuQ_4−LnQ_6) sequence as the three center polyhedra and include an extra LnQ_6 octahedron on either end. The LnQ_6 octahedra at the ends of the three- and five-polyhedron sequences connect in an edge-sharing manner to form the sides of the tunnel. This edge-sharing connection between layers results in a square planar Q site on either side of the tunnels and causes puckering in the corrugated layers to form the 3D framework.

The n = 2 $Rb_2Cu_4Dy_2S_9$ compound shown in Figure 1B crystallizes in the $Rb_2Cu_4Gd_4S_9$ structure type[15] with the $C2/m$ space group. The structure is formed from LnQ_6 octahedra and CuQ_4 tetrahedra with similar connectivity to the n = 1 structure forming a 3D anionic framework with one alkali metal-wide tunnels. An extra Cu_2Q equivalent is incorporated

https://doi.org/10.1021/acs.chemmater.2c00223
Chem. Mater. 2022, 34, 3409−3422

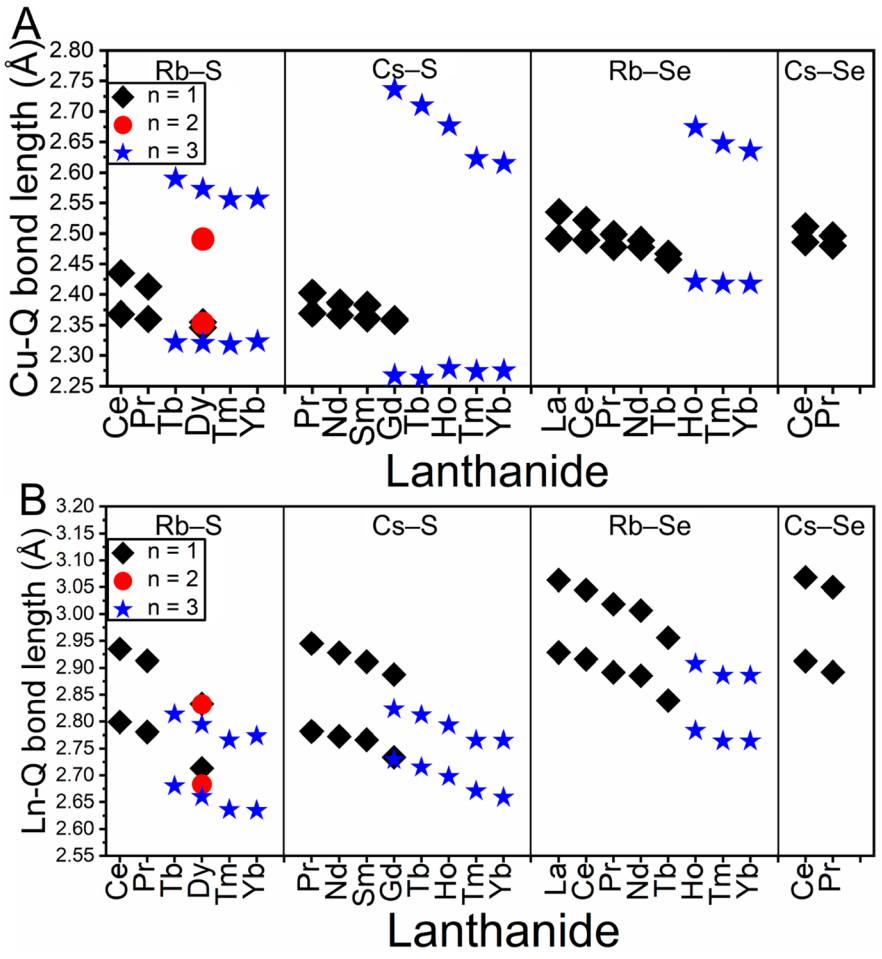

Figure 4. Range of (A) Cu−Q and (B) Ln−Q bond lengths for each compound reported for the n = 1 (black diamonds), n = 2 (red circles), and n = 3 (blue stars) series. The increased range of Cu−Q bond lengths in the n = 3 structure reflect the distortions occurring in the structure which correlate with larger alkali metals and larger lanthanides.

at the square planar Q sites in the framework between the layers. This incorporation replaces half the Q square planar sites with two edge-sharing CuQ_4 tetrahedra while still forming tunnels with eight polyhedra (Figure 2B) and mildly distorts the alkali metal environment (Figure 3B). The tunnel is still formed with three polyhedra (LnQ_6−CuQ_4−LnQ_6) on top and bottom of the tunnel as in the n = 1 structure, but one of the added CuQ_4 tetrahedra has displaced one of the LnQ_6 on one side of the tunnel. The other side of the tunnel wall still has an edge-sharing LnQ_6 from the adjacent layers, forming a square planar Q site unchanged from the n = 1 structure. This results in a repeating sequence of one square planar Q site, one alkali metal, and one CuQ_4 tetrahedron along the [001] direction.

The $ACu_3Ln_2Q_5$ compounds reported here crystallize in the n = 3 ($A_2Cu_6Ln_2Q_{10}$) $RbAg_3Sm_2Se_5$ structure type[16] with the *Cmcm* space group shown in Figure 1C. The final member of the homologous series once again incorporates an additional Cu_2Q equivalent into the 3D anionic framework in a similar manner to that of the n = 2. The additional Cu_2Q equivalent replaces the remaining square planar Q sites in the n = 2 structure with another pair of edge-sharing CuQ_4 tetrahedra between the layers. The perimeter of the tunnel now has the 3-polyhedra unit (LnQ_6−CuQ_4−LnQ_6) on the top and bottom of the tunnel, with CuQ_4 tetrahedra on both sides. This results in eight polyhedra alternating between LnQ_6 and CuQ_4 around the tunnel, as shown in Figure 2C, and the alkali metal coordination environment returns to the undistorted AQ_8 polyhedra observed in the n = 1 structure, as shown in Figure 3C. The final addition of Cu_2Q fully converts the connected corrugated layers into a purely 3D framework, completing the homologous series.

A close examination of the copper tetrahedra in these structures indicates that some distortion occurs, primarily in the $ACu_3Ln_2Q_5$ n = 3 structure type. This can be seen in the range of Cu−Q bond lengths for each compound, as shown in Figure 4A. There is little distortion in all the n = 1 structures, as reflected in the nearly ideal tetrahedra seen in both $CsCuGd_2S_4$, which exhibit Cu−S bond lengths that range from 2.357(3) to 2.360(3) Å, and in $RbCuDy_2S_4$, in which the bond lengths range from 2.346(4) to 2.355(5) Å. The n = 2 $Rb_2Cu_4Dy_4S_9$ exhibits some distortion in the copper tetrahedra, in which the Cu−S bond length ranges from 2.353(4) to 2.491(6) Å. The most pronounced distortions occur in the n = 3 structures, in which the Cu−S bond length in $RbCu_3Dy_2S_5$ ranged from 2.3202(10) to 2.5731(13) Å, and in $CsCu_3Gd_2S_5$, in which they range from 2.267(3) to 2.736(4) Å. It is notable that for both the n = 2 and the n = 3 structures, copper has two different Wyckoff sites, and this distortion is only observed in one of the two sites. The copper site exhibiting the distortion is the one already present in the framework in the n = 1 structure, while the copper site formed

https://doi.org/10.1021/acs.chemmater.2c00223
Chem. Mater. 2022, 34, 3409−3422

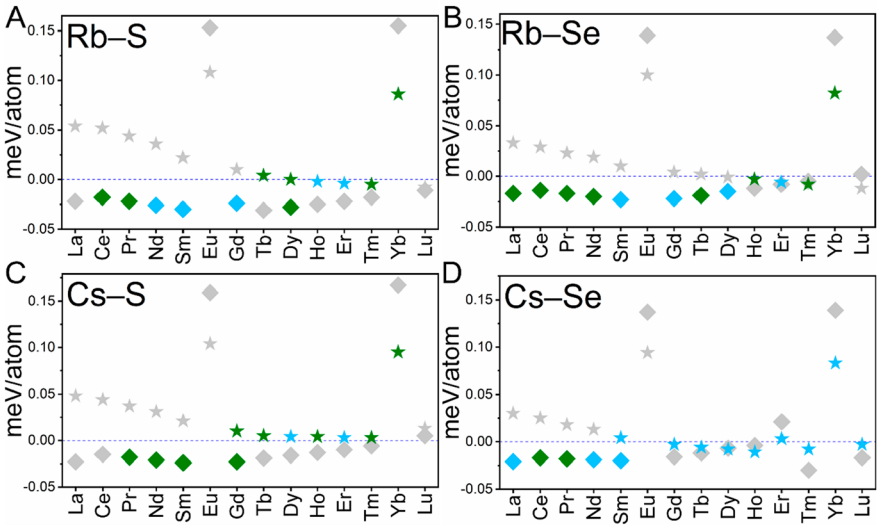

Figure 5. DFT stability calculation results for n = 1 (diamonds) and n = 3 (stars) for (A) Rb/Cu/Ln/S, (B) Rb/Cu/Ln/Se, (C) Cs/Cu/Ln/S, and (D) Cs/Cu/Ln/Se. Gray indicates no experimental report, green indicates experimental reports from this work, and blue indicates experimental reports from other works.

due to the additional Cu_2Q does not exhibit considerable distortion. The degree of distortion seen in the copper tetrahedra increases with decreasing atomic number of the lanthanide (as the lanthanide gets larger) and with increasing alkali metals size. However, the degree of distortion remains relatively constant between sulfur and selenium. This distortion may result from the larger cations forcing the 3D framework to buckle, and the lowest energy method to accomplish this is by distorting the copper tetrahedra.

For all three structures, the lanthanide octahedra show only minor distortions. The Ln−Q bond length shows a decreasing trend with increasing atomic number of the lanthanide, as expected (Figure 4B). The longest bonds are observed in the n = 1 $RbCuLa_2Se_4$ ranging from 2.9285(11) to 3.0631(7) Å and the shortest in $RbCu_3Yb_2S_5$ ranging from 2.6347(17) to 2.773(3) Å. The range of Ln−Q bond lengths for each of the three structure types remains relatively constant for a given alkali metal for both sulfides and selenides. Changing the alkali metal does change the range of Ln−Q bond lengths by ∼0.03 Å for the whole series. For the n = 1 structure type, the Rb analogues have a shorter range of Ln−Q bond lengths of ∼0.13 Å while the Cs analogues have a range of ∼0.16 Å. Similarly, in the n = 3 structures, the Rb analogue range of the Ln−Q bond lengths is smaller at ∼0.10 Å compared to ∼0.13 Å for the Cs analogues.

Synthesis and Crystal Growth. $A_2Cu_{2n}Ln_4Q_{7+n}$ (n = 1, 2, 3) crystals suitable for single-crystal X-ray diffraction were grown using alkali metal halide salt fluxes in graphite crucibles and graphite lids with three layers of carbon coating. It was necessary that both the crucible and lids be made of graphite with the carbon coating because of the observed formation of the orange silicate Ce_2SiO_4Se[49] inside the crucible during the reaction targeting $CsCuCe_2Se_4$, where the carbon coatings had not been used. Scanning electron microscopy (SEM) and energy dispersive spectroscopy (EDS) data of the Ce_2SiO_4Se are provided in the SI. CsCl was used exclusively for Cs-containing reaction targets, whereas either RbCl or RbBr were used for the synthesis of Rb compounds.

In general, the reagents A_2Q:Cu:Ln:Q were loaded in a stoichiometric ratio of either 1:2:4:7 for $ACuLn_2Q_4$ or 1:6:4:9 for $ACu_3Ln_2Q_5$. The salt was then added in a 10:1 ratio to the mixture. Two of these reactions yielded multiple members of the homologous series in a single reaction. The first reaction was targeting n = 3 $RbCu_3Dy_2S_5$, which resulted in n = 1, 2, and 3 phases in the Rb/Cu/Dy/S system. The second reaction was targeting n = 3 $CsCu_3Gd_2S_5$ which resulted in n = 1 and 3 phases in the Cs/Cu/Gd/S system. These flux reactions typically yield side products; however, the target phase is identifiable as the only needles present: either the red needles for the sulfides or black needles for the selenides except $CsCuPr_2S_4$ (orange needles). When multiple members of the homologous series form in a single reaction, the different members are indistinguishable and cannot be separated. The side products identified from these reactions were all similar. Various Cu/Q binaries were observed, always at the bottom of the crucible as irregularly shaped black clumps, whereas some Ln_2Q_3 binary compounds were often found at the top of the product in the crucible. The target phase, along with various ternaries, was observed in the center of the crucible, with the salt flux crystallizing everywhere in the crucible. $ALnQ_2$, $CuLnQ_2$, and $A_3Er_7Q_{12}$ were also found in the center with unidentified minor phases. The salt flux was removed by methanol sonication, and the supernatant liquid was decanted until no white material was present. Then, the remaining solid products were dried under a nitrogen stream. The needles were mechanically separated for single-crystal experiments and selected for additional characterization. SEM with an EDS attachment was used to confirm the elemental composition of each phase; the data is presented in the Supporting Information.

Comparison of Experimental and DFT-Calculated Thermal Stabilities. The thermal stability was studied experimentally using differential thermal analysis (DTA) and theoretically using high-throughput DFT calculations. The DTA experiments were used to assess high-temperature stability under static vacuum for $RbCuNd_2Se_4$, $RbCuTb_2Se_4$, and $RbCu_3Tb_2S_5$ in sealed fused silica ampules. The DTA and powder X-ray diffraction (PXRD) data before and after heating are provided in the Supporting Information. The n = 1 members showed no thermal events up to 1000 °C (heating

https://doi.org/10.1021/acs.chemmater.2c00223
Chem. Mater. 2022, 34, 3409−3422

rate: 10 °C/min) and appeared physically unchanged, and their PXRD data were the same before and after the DTA, indicating thermal stability up to 1000 °C. The n = 2 $Rb_2Cu_4Dy_4S_9$ could not be isolated for property measurements because of the presence of both n = 1 and n = 3 members, which are visually indistinguishable red needles. The n = 3 $RbCu_3Tb_2S_5$ also showed no reproducible melting events and appeared unchanged after DTA, both visually and as confirmed by PXRD.

The thermodynamic stability of the n = 1 and n = 3 structures at 0 K was examined using high-throughput DFT calculations for the Cs/Cu/Ln/Q and Rb/Cu/Ln/Q compositional phase spaces, where Ln = La to Lu except *Pm*, as shown in Figure 5 for Q = S and Se and in the SI for Q = O and Te and n = 2. The analogous potassium space was not examined due to the number of synthetic targets already present for Cs and Rb, but potassium containing phases are present in this structural family.[12−14,18] The stability (defined in the Experimental Methods section) calculated in OQMD was used to evaluate the thermodynamic stability of the n = 1, 2, or 3 phases at 0 K for each four-element compositional space. This means that all the phases with a zero or negative calculated energy are predicted to be thermodynamically stable.

The calculation results for the oxides and tellurides and for the n = 2 structure are provided in Figures S11 and S12 in the Supporting Information. All oxides for all three structure types were found to be unstable, and we did not attempt to synthesize them. This is expected as chalcogenides (S, Se, Te) often form structures that are different from those of oxides and often have different competing phases, which is consistent with the fact that no oxygen-containing compounds have been reported in this family.

For the telluride-based compositions, our calculations showed that the n = 1 structure type was generally stable, while the n = 3 structure type was lying either just below or just above the convex hull (the convex hull without considering the target phase). However, because of the large number of synthetic targets for sulfides and selenides, tellurides were not targeted in this work. It should be noted, however, that few experimental reports exist for quaternary compounds in the A/Cu/Ln/Te composition space, and most of the reported ones have different stoichiometries, such as the layered $Cs_2Cu_3DyTe_4$[50] or 3D tunnel framework $Cs_3Cu_5Gd_4Te_{10}$.[1] The two reported compounds $CsCuY_2Te_4$[51] and $CsCuGd_2Te_4$[11] are isostoichiometric but are not isostructural to the n = 1 $ACuLn_2Q_4$ structure type examined here. They have a different 3D framework which incorporates a two alkali metal-wide tunnel instead of a one alkali metal-wide tunnel. This experimentally observed $ACuLn_2Te_4$ structure type is therefore more likely to be observed experimentally than the n = 1 $ACuLn_2Q_4$ structure type for tellurides. Further exploration of the telluride compositional space is required to determine which structures can be realized experimentally.

The calculation results for the sulfide and selenide compositional spaces are separated into the four groups shown in Figure 5 based on alkali metal (Rb or Cs) and chalcogenide (S or Se). The observed general trend is that, for a given alkali metal and chalcogenide, the $ACuLn_2Q_4$ n = 1 phase is stable but becomes slightly less stable with increasing atomic number of the lanthanide, whereas the $ACu_3Ln_2Q_5$ n = 3 phase is unstable for light lanthanides but eventually becomes stable as the atomic number of the lanthanide increases. Additionally, for sulfides, the two phases become nearly equally stable, while for selenides, the n = 3 phase is predicted to become more stable than the n = 1 phase by the end of the lanthanide series. This converging stability behavior coincides well with the synthetically observed trend of n = 1 phases for lighter lanthanides, n = 3 phases for heavier lanthanides, and multiple structures observed with lanthanides from the middle of the series from a single reaction, such as for Rb/Cu/Dy/S and Cs/Cu/Gd/S compositional spaces. The calculated stabilities of the n = 2 phase show the same trend as those for the n = 3 phase, as illustrated in Figures S11 and S12. For both of the Rb groupings, all three phases of the homologous series are predicted to be stable when the lanthanide was Dy through Tm. This fact along with the success of synthesizing all three phases for Rb/Cu/Dy/S indicates it can be possible to synthesize additional homologous members.

However, a few selected compositions do not follow the observed trend. For the Eu and Yb analogues, our calculations showed that both structure types are unstable. They exhibit 2^+ oxidation states much more frequently than the other lanthanides because this oxidation state results in either half-full or full f electron orbitals. The 2^+ oxidation state results in different competing phases and a convex hull energy landscape that is different from those of the other lanthanides. While the synthesis of Eu compounds was not attempted in this study, three new Yb-based $ACu_3Yb_2Q_5$ n = 3 compounds were successfully synthesized. These results along with the reported $CsCu_3Yb_2Se_5$[21] mean that all four Yb-containing n = 3 sulfide and selenide phases have been obtained synthetically despite our DFT calculation results predicting that they are thermodynamically unstable. This is because the OQMD assumed the Eu- and Yb-containing compounds to be in the 2^+ oxidation state, which resulted in the convex hull constructions being different from when Eu and Yb exhibit the 3^+ oxidation state, as was the case in this study. The *Pm* composition was excluded from this study because *Pm*-based materials are relatively underexplored owing to their radioactivity.

The last deviation occurs for the Cs/Cu/Er/Se composition (Figure 5D), in which both phases are slightly unstable. This can be explained by examining the differences between the competing phases for Cs/Cu/Er/Se and the rest of the composition space. For both Cs/Cu/Ce/S and Cs/Cu/Er/S as examples, the competing phases are $CsLnS_2$, Ln_2S_3, and $CsCu_3S_2$. However, the existence of $CsEr_3Se_5$ in the Cs/Cu/Er/Se composition space results in the lower energy combination of competing phases of $CsEr_3Se_5$ and $CsCu_3Se_2$. This additional ternary competing phase is just stable enough to cause $CsCuEr_2Se_4$ and $CsCu_3Er_2Se_5$ to lie above the convex hull. Therefore, $CsCu_3Er_2Se_5$ is predicted to be metastable, and we were able to synthesize $CsCu_3Er_2Se_5$ in this study.

Examining the synthetic preferences for the n = 1 versus n = 3 phases as a function of the lanthanide in the four different compositional ranges yields similar but different crossover points. These crossover points observed from synthesis for Rb/S are Gd (n = 1) to Tb (n = 3), for Rb/Se are Dy (n = 1) to Ho (n = 3), for Cs/S is Gd (n = 1 and 3), and for Cs/Se is Sm (n = 1 and 3). A close examination of the Rb/Cu/Ln/S compositional series (Figure 5A) reveals that the first lanthanide in the n = 3 structure of Tb was predicted to be only 0.04 eV/atom above the convex hull. In contrast, for the Rb/Cu/Ln/Se series, the first lanthanide in the n = 3 structure is Ho, and it was predicted to be stable. For both the Cs/Cu/

https://doi.org/10.1021/acs.chemmater.2c00223
Chem. Mater. 2022, 34, 3409−3422

Ln/S and the Cs/Cu/Ln/Se compositional series, the crossover point occurs with both the n = 1 and the n = 3 structure observed for one lanthanide. For Cs/Cu/Ln/S, this crossover occurs with Gd where the n = 3 structure was only 0.01 eV/atom above the convex hull. For Cs/Cu/Ln/Se series, this crossover occurs with Sm where the n = 1 $CsCuSm_2Se_4$ was synthesized by Huang and Ibers[15] while the n = 3 $CsCu_3Sm_2S_5$ synthesized by Strobel and Schleid[21] was only 0.04 eV/atom above the convex hull.

The n = 3 structure shows the trend of starting to form with lighter lanthanides for Cs compositions than for Rb compositions. This is likely explained by the fact that larger Cs better fills the tunnel than Rb, enabling the formation of the n = 3 structure type with larger lanthanides. The only compound in one of these compositional series that was not identified resulting in a gap as the lanthanide atomic number increases is for the Rb/S series in the n = 1 structure with Tb. It is likely that the unidentified composition $RbCuTb_2S_4$ could be synthesized with further efforts. This is because it is predicted to be thermodynamically stable; the n = 1 $RbCuDy_2S_4$, which is one atomic number higher than Tb, was successfully synthesized, and the n = 3 phase $RbCu_3Tb_2S_5$ was identified synthetically.

Electronic and Optical Properties. The optical properties of selected materials were studied using UV−vis diffuse reflectance spectroscopy and PYSA. The diffuse reflectance data were transformed using the Kubelka−Munk transformation[52] into absorbance data, and the absorption edge was then determined by extrapolating the linear region to determine the intercept, as shown in Figure 6A. The work

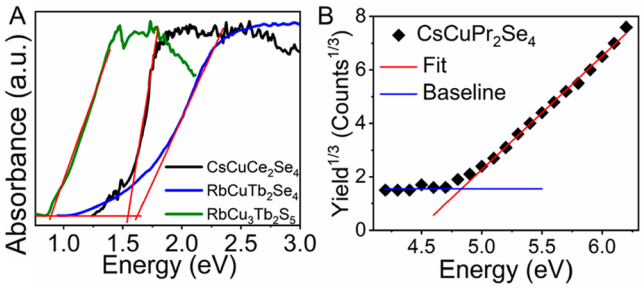

Figure 6. (A) Optical absorption spectra of $CsCuCe_2Se_4$ (black) with a band gap of 1.55(5) eV, $RbCuTb_2Se_4$ (blue) with a band gap of 1.62(5) eV, and $RbCu_3Tb_2S_5$ (green) with a band gap of 0.90(5) eV. (B) Photoemission yield spectra in air of $CsCuPr_2Se_4$ with a valence band maximum of 4.83(5) eV.

function, which is the valence band maximum (VBM) with respect to the vacuum energy, was determined from the PYSA data by extrapolating the linear region and finding the intercept, as shown in Figure 6B. Based on the absorption spectra, the band gaps of $CsCuCe_2Se_4$, $RbCuTb_2Se_4$, and $RbCu_3Tb_2S_5$ are found to be 1.55(5), 1.62(5), and 0.90(5) eV, respectively. Based on the PYSA data, the VBM of $CsCuPr_2Se_4$ is found to be 4.83(5) eV.

The electronic band structure and partial density of states (PDOS) were calculated for the selected compounds and are summarized in Figures S15 and S16 in the SI. All three different structure types, the n = 1 phase (Figures 7A,B), n = 2 phase (Figure 7C), and n = 3 phase (Figure 7D), were predicted to be indirect gap semiconductors. The valence band maximum occurs at the Γ point for all three types, while the conduction band minimum (CBM) occurs at the S point for the n = 1 and 3 structures and the M/N point for the n = 2 structure. Because the n = 1 or 3 (space group $Cmcm$) and n = 2 structures (space group $C2/m$) adopt different space groups, the k-point paths are different between the n = 1 or n = 3 structures and the n = 2 structure. All three structure types have a dispersive conduction band (∼1 eV). The shapes of the band structures are similar for the same structure type (e.g., all n = 1 phases), as seen from Figures 7, S15, and S16; however, different Cs/Rb, Ln, and Q elements result in some localized differences in the band structures. For example, the VBM in $CsCuCe_2Se_4$ shows band convergence at the R and Γ points (Figure 7A), whereas this convergence is absent in $RbCuCe_2Se_4$ (Figure 7B). The effective masses were calculated for all four structures, as illustrated in Figure 7 and Table 4. As observed from the band structures, the effective masses were similar among the n = 1 and n = 3 structures. For the CBM, the highest dispersion and smallest calculated effective mass are along the S−X direction. For the VBM, the highest dispersion and smallest calculated effective mass are along the Γ−Y direction. For the n = 2 structure, the CBM dispersion is highest in the Γ−X direction and nearly as high in the Z−I_1 direction. The minimum effective mass of the holes is in the Γ−X direction, which is the most dispersive direction in the VBM.

Phonon Dispersion and Dynamic Stability. The phonon dispersion and phonon density of states (DOS) were calculated for the selected compounds and are summarized in Figures S17 and S18 in the SI. All the n = 1 or 2 structures are predicted to be dynamically stable at T = 0 K, and two examples, $CsCuCe_2Se_4$ and $Rb_2Cu_4Dy_4S_9$, are shown in Figure 8A,B, respectively. The low frequencies of the acoustic phonon branches possibly result in the low lattice thermal conductivity of $CsCuCe_2Se_4$. The calculated n = 2 structure (Figure 8B) is also dynamically stable at T = 0 K. A number of the n = 3 structures, however, exhibit negative phonon modes but not all of them (Figure 8C,D). Negative-frequency phonons indicate that the structure is dynamically unstable at T = 0 K and that a structural phase transition may occur at low temperatures.

A detailed investigation on the representative compound $RbCu_3Tb_2S_5$, which had imaginary phonon modes (Figure 9D), revealed that it is not dynamically stable at T = 0 K. The atomic vibration directions at the Γ point in the original n = 3 structure ($Cmcm$) are shown in Figure 9B. This vibration causes some of the copper atoms to distort from the copper tetrahedra toward a trigonal planar copper geometry (Figure 9C). A fully relaxed structure with lower symmetry ($Cmc2_1$) is obtained by allowing these copper atoms to move along the force constant matrix eigenvectors of the lowest unstable phonon, which is predicted to be dynamically stable at T = 0 K (Figure 9F). This finding suggests that a phase transformation from $Cmcm$ to $Cmc2_1$ occurs in $RbCu_3Tb_2S_5$ at low temperatures. As shown in Figure 9E, the renormalized phonon dispersion demonstrates that the original n = 3 structure of $RbCu_3Tb_2S_5$ is dynamically stabilized at room temperature.

Distorted copper tetrahedra are observed in some n = 3 structures, which may induce dynamic instability in these structures. We define the distortion index of a copper tetrahedron as $D = \sum_{i=1}^{4} \frac{\mathrm{abs}(d_i - \bar{d})}{\bar{d}}/4$, where d_i is the bond length of each Cu−Q pair and $\bar{d}$ is the average bond length. D has the units of bond length, and a larger D indicates a greater

https://doi.org/10.1021/acs.chemmater.2c00223
Chem. Mater. 2022, 34, 3409−3422

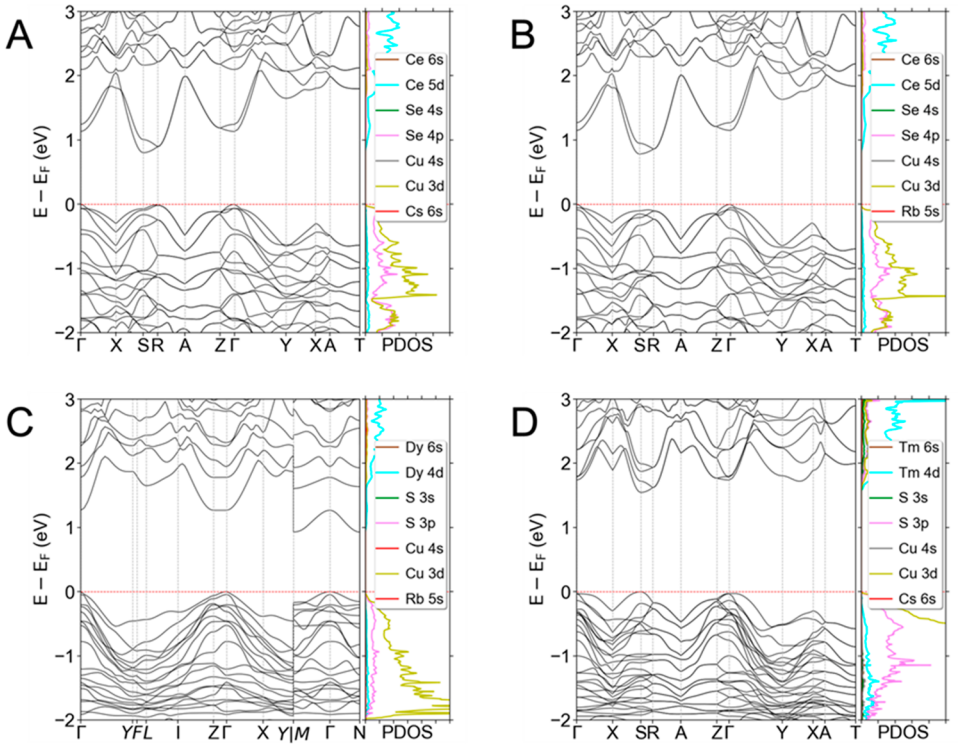

Figure 7. Electronic band structures for (A) $CsCuCe_2Se_4$ (n = 1), (B) $RbCuCe_2Se_4$ (n = 1), (C) $Rb_2Cu_4Dy_4S_9$ (n = 2), and (D) $RbCu_3Tm_2S_5$ (n = 3).

Table 4. Effective Masses at CBM and VBM of $CsCuCe_2Se_4$, $RbCuCe_2Se_4$, $Rb_2Cu_4Dy_4S_9$, and $RbCu_3Tm_2S_5$ Compounds[a]

direction	$CsCuCe_2Se_4$	$RbCuCe_2Se_4$	$RbCu_3Tm_2S_5$	direction	$Rb_2Cu_4Dy_4S_9$
			Electrons		
S → X (E)	0.410	0.415	0.427	Z → I_1 (E)	0.964
S → R (E)	1.684	1.969	1.553	Z → Γ (E)	Inf
Γ → Z (E)	2.634	2.255	0.482	Γ → Z (E)	Inf
Γ → Y (E)	0.846	0.892	0.362	Γ → X (E)	0.971
			Holes		
R → S (H)	−1.243	−1.486	−2.336	Γ → M (H)	−2.184
R → A (H)	−1.635	−2.232	−7.843	Γ → N (H)	−1.869
Γ → Z (H)	−1.130	−1.176	−1.364	Γ → Z (H)	−1.718
Γ → Y (H)	−0.604	−0.572	−0.677	Γ → X (H)	−1.052

[a]Effective mass is provided in units of m_0. E and H indicate effective mass of the electron and hole in the given direction, respectively.

extent of distortion. For example, D is 0.078 in the original structure of $RbCu_3Tb_2S_5$ for the distorted copper tetrahedra (green arrows in Figure 9A) and 0.017 for the other copper tetrahedra that do not exhibit the negative phonon mode.

To quantify the extent of dynamic instability, fully relaxed structures were generated by allowing atom movement in the direction of atom vibrations at the Γ point (Figure 9B) for $ACu_3Ln_2Q_5$ structures, where A = Cs/Rb, Ln = Gd/Tb/Dy/Ho/Er/Tm, and Q = S/Se. The energy difference between the original and the fully relaxed structures is denoted as $E_{origin} - E_{mod}$, and it is plotted against the lowest phonon frequency for the 24 structures. In statistics, the coefficient of determination (R^2) measures the correlation between the observed outcomes and the observed predictor values, and a value close to 1 means two variables are closely related, while a value close to 0 means they are unrelated. The $E_{origin} - E_{mod}$ is linearly related to the lowest phonon frequency with an R^2 of 0.81 and a quadratic relationship with an R^2 of 0.85 (as shown in Figure 10A), demonstrating that these two parameters are monotonically related. In the following discussion, $E_{origin} - E_{mod}$ is used to describe the dynamic instability of a compound. The relationship between the distortion index and dynamic instability is illustrated in Figure 10B, which shows the strong linear relationship within each Cs/Q or Rb/Q group. Overall, a linear fit with an R^2 of 0.65 was obtained for all data points, verifying our assumption that the larger distortion in copper tetrahedra causes the larger dynamic instability in these structures. The question remains whether it is possible to predict a compound's dynamic instability using only compositional properties (i.e., atomic radius, ionic radius, electronegativity difference, and lanthanide atomic number). The plots of all four properties and their variants (e.g., ratio of two properties) are provided in Figure S19 in the SI, and the electronegativity of the Ln elements (Figure 10C) showed the highest linear correlation with the dynamic instability of the structures among all these properties. The trend between the different elements and distortion in the copper tetrahedra discussed in the Structure and Homologous Relationship

https://doi.org/10.1021/acs.chemmater.2c00223
Chem. Mater. 2022, 34, 3409−3422

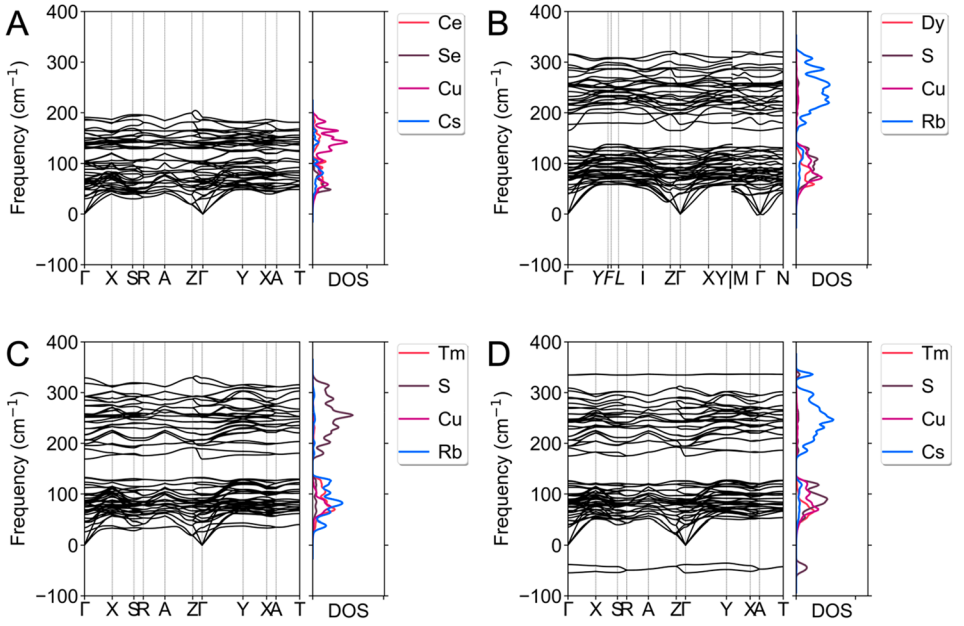

Figure 8. Phonon dispersions and phonon density of states for (A) $CsCuCe_2Se_4$ (n = 1), (B) $Rb_2Cu_4Dy_4S_9$ (n = 2), (C) $RbCu_3Tm_2S_5$ (n = 3), and (D) $CsCu_3Tm_2S_5$ (n = 3). The last one exhibits negative phonon modes caused by a copper atom.

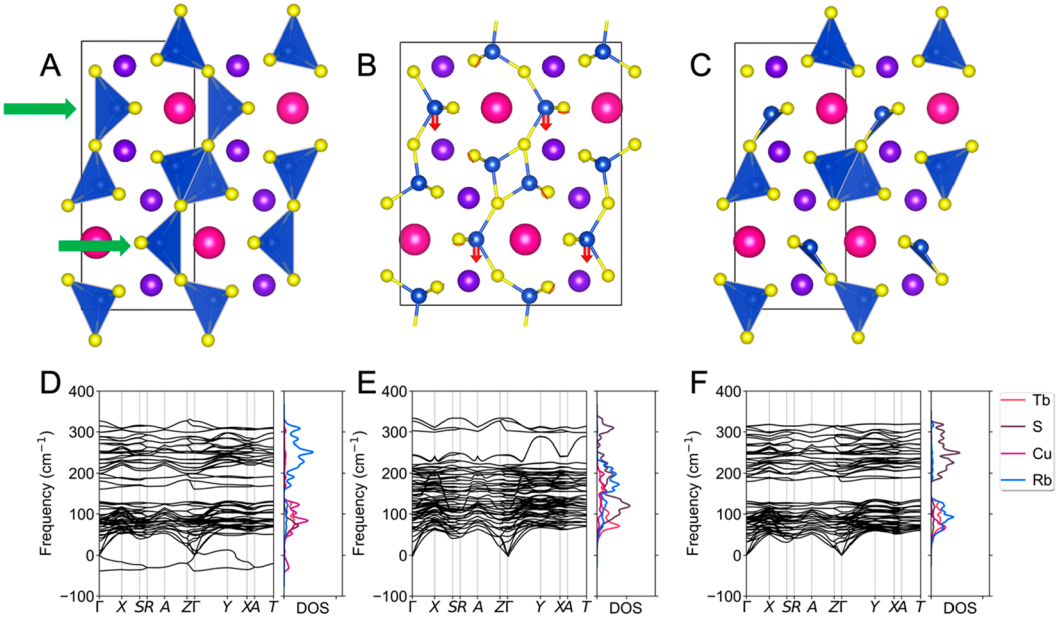

Figure 9. Original structure of $RbCu_3Tb_2S_5$ (n = 3). (A) Green arrows indicate distorted copper tetrahedra. (B) Atom vibrations at the Γ point in the $RbCu_3Tb_2S_5$ (n = 3) structure. The negative phonon modes (D) indicate that this structure is not dynamically stable at T = 0 K. (E) Phonon dispersion calculated at T = 300 K indicating that the structure is dynamically stable at finite temperature. (C) Fully relaxed structure of $RbCu_3Tb_2S_5$ where Cu atoms moved in the directions of the atom vibrations shown in (B). (F) Phonon dispersion demonstrating that the structure is dynamically stable at T = 0 K.

section is shown in Figure 10D, where the atomic number of the lanthanides is plotted against dynamic instability. With decreasing lanthanide atomic number or increasing alkali metal atomic number, the degree of distortion in the copper tetrahedra becomes larger, and the structure tends to be more dynamically unstable (i.e., larger $E_{origin} - E_{mod}$). This indicates that the dynamic instability in the n = 3 structures can be best explained by the size of the alkali metal and lanthanide. This can be chemically understood as the larger Cs applying more chemical pressure on the framework than the smaller Rb and the larger lanthanides exerting higher steric strain on the framework than the smaller ones. The lowest energy relaxation for the framework is to allow the copper to distort via a shift toward a trigonal planar copper position.

Single-crystal data were collected at 6 and 480 K in addition to the 293 K room-temperature data for $CsCu_3Tb_2S_5$ to investigate evidence of this distortion. Given that the structure is predicted to be in the *Cmcm* space group at these three

https://doi.org/10.1021/acs.chemmater.2c00223
Chem. Mater. 2022, 34, 3409−3422

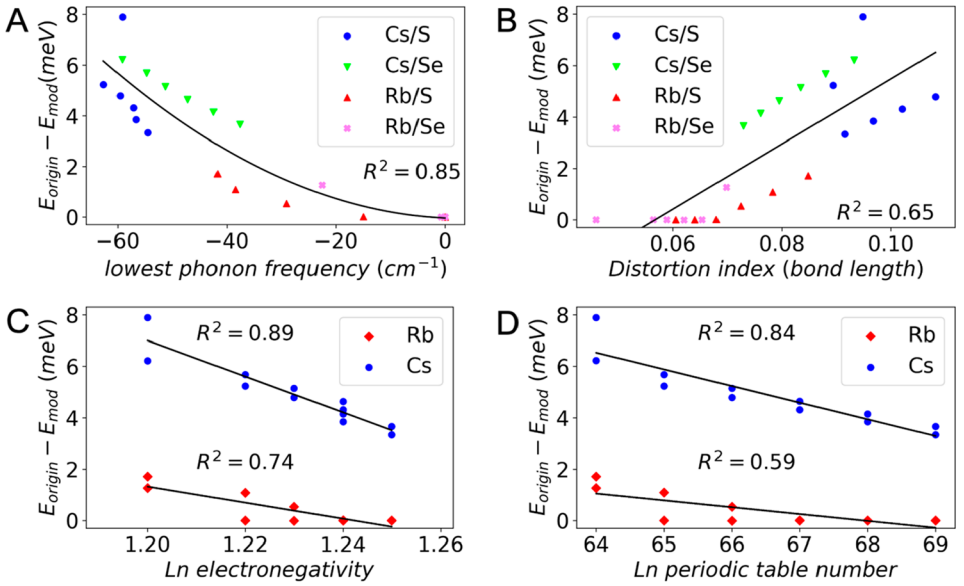

Figure 10. Relationships between $E_{origin} - E_{mod}$ (i.e., the energy difference between the original and fully relaxed structures) and (A) lowest phonon frequency, (B) distortion index, (C) Ln electronegativity, and (D) Ln periodic table number for $ACu_3Ln_2Q_5$ structures where A = Cs/Rb, Ln = Gd/Tb/Dy/Ho/Er/Tm, and Q = S/Se.

temperatures, the anisotropic displacement parameters of this copper site (Cu2) (listed in Tables S77, S80, and S83) indicates unusual behavior. Notably, U_{33} is elevated at all temperatures with values of 36(2), 71(3), and 91(2) Å$^2 \times 10^3$, resulting in the elongation of the copper ellipsoid along the *c* direction, which is expected if the copper is beginning to transition toward a trigonal planar geometry, as predicted. These values are approximately three times higher than those for U_{33} for the other copper sites in the structure. Attempts to refine the data in the predicted space group $Cmc2_1$ by removing the mirror plane made the copper move off the center of the tetrahedral site, resulted in worse refinements, and did not result in substantive movement of the center of the copper site toward a trigonal planar position. In addition, for the 6 K data set, restraints were required to obtain a stable model. Therefore, we conclude that the predicted change to an ordered trigonal planar site does not occur at 6 or 480 K. This does not exclude the possibility of short-range ordering, where the copper position may either be off-center to one side in a random manner or have moved to the trigonal planar position to either side in a random manner, resulting in the average crystallographic position being at the tetrahedral site. Additional X-ray studies using the pair distribution function or other techniques are required to further examine this aspect. Additionally, this does not exclude the possibility of the off-centering in one of the other $n = 3$ compounds that exhibits negative phonon modes.

Calculated Thermoelectric Properties. The potential of $A_2Cu_{2n}Ln_4Q_{7+n}$ compounds $CsCuCe_2Se_4$ as thermoelectric materials was investigated. The lattice thermal conductivity of $CsCuCe_2Se_4$ is predicted to be very low (Figure 11), particularly along the *c* direction of the crystal structure, which is the direction in which the channels propagate. However, the electrical conductivities were largest in the *a* direction and smallest in the *c* direction. The band structures around the conduction band minimum indicate that the difference in the electrical conductivities in these two directions is a consequence of the much steeper band along

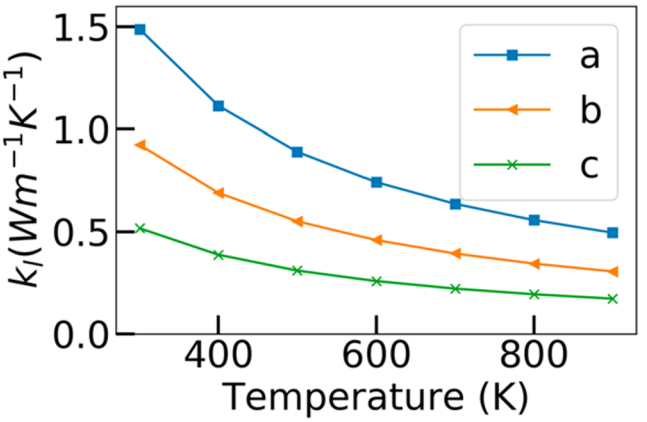

Figure 11. Calculated thermal conductivity of $CsCuCe_2Se_4$ along the *a*, *b*, and *c* crystal axes.

the S−X (*a* direction) direction than along the S−R (*c* direction) direction. This leads to a much smaller electron effective mass, and thus, a much higher electron mobility, along the *a* direction. BoltzTraP was used to calculate the electrical conductivity and carrier thermal conductivity with three constant relaxation times (5, 10, and 20 fs). The results are compared with those derived using AMSET. Although the lattice thermal conductivity is predicted to be the lowest in the *c* direction, the power factor in this direction is also predicted to be very low because of the poor electrical conductivity; thus, the overall ZT is predicted to be low, as shown in Figures S20 and S21. The highest ZT value is predicted to be along the *a* direction, reflecting high electrical conductivity. For example, $CsCuCe_2Se_4$ is predicted to be an n-type thermoelectric material with a ZT as high as 0.15 at 300 K and 0.75 at 600 K.

CONCLUSION

Twenty-seven new members of the homologous series $A_2Cu_{2n}Ln_4Q_{7+n}$ (A = Cs, Rb; Ln = La−Nd, Sm, Gd−Yb; Q = S, Se) were synthesized. For each increment in *n*, one Cu_2Q

https://doi.org/10.1021/acs.chemmater.2c00223
Chem. Mater. 2022, 34, 3409−3422

was incorporated into the 3D framework as an edge-sharing copper tetrahedron to replace the square planar chalcogenide sites. High-throughput DFT calculations predicted many of the phases to be thermodynamically stable. These predictions were compared with the synthesis results for the phases formed in each composition space. With increasing lanthanide atomic number, the $n = 3$ $ACu_3Ln_2Q_5$ showed better agreement with the DFT calculations, which predicted the $n = 3$ phase to be stable. The DTA for the selected $n = 1$ phases $RbCuNd_2Se_4$ and $RbCuTb_2Se_4$ was found to be thermally stable under vacuum up to 1000 °C. Optical measurements were performed on $CsCuCe_2Se_4$ and $RbCuTb_2Se_4$ as representatives of the class, and their band gaps were found to be 1.55(5) and 1.62(5) eV, respectively. Additionally, some members of the $n = 3$ $ACu_3Ln_2Q_5$ structure type were calculated to have negative phonon modes in the phonon-dispersion calculations, indicating that the structures exhibit dynamic instability. This negative phonon mode vibration pushes the copper at one of the two copper Wyckoff positions to distort the copper tetrahedra toward a trigonal planar-like copper geometry. A linear relationship was observed between the dynamic instability of the structures and the atomic numbers of the lanthanides.

■ ASSOCIATED CONTENT

Supporting Information

The Supporting Information is available free of charge at https://pubs.acs.org/doi/10.1021/acs.chemmater.2c00223.

Additional experimental details, full crystallographic tables, SEM and EDS, differential thermal analysis, powder X-ray diffraction, DFT stability, band structure, phonon structures, and calculated thermoelectric properties (PDF)

X-ray crystallographic data for CSD deposit numbers 2143709−2143737 (ZIP)

■ AUTHOR INFORMATION

Corresponding Author

Mercouri G. Kanatzidis − *Department of Chemistry, Northwestern University, Evanston, Illinois 60208, United States; Materials Science Division, Argonne National Laboratory, Lemont, Illinois 60439, United States;* orcid.org/0000-0003-2037-4168; Email: m-kanatzidis@northwestern.edu

Authors

Craig C. Laing − *Department of Chemistry, Northwestern University, Evanston, Illinois 60208, United States;* orcid.org/0000-0002-0654-4741

Jiahong Shen − *Department of Materials Science and Engineering, Northwestern University, Evanston, Illinois 60208, United States;* orcid.org/0000-0002-1951-2183

Michael A. Quintero − *Department of Chemistry, Northwestern University, Evanston, Illinois 60208, United States;* orcid.org/0000-0002-0709-1676

Benjamin E. Weiss − *Department of Chemistry, Northwestern University, Evanston, Illinois 60208, United States*

Yi Xia − *Department of Materials Science and Engineering, Northwestern University, Evanston, Illinois 60208, United States*

Zhi Li − *Department of Materials Science and Engineering, Northwestern University, Evanston, Illinois 60208, United States;* orcid.org/0000-0003-0451-567X

Jiangang He − *Department of Materials Science and Engineering, Northwestern University, Evanston, Illinois 60208, United States*

Chris Wolverton − *Department of Materials Science and Engineering, Northwestern University, Evanston, Illinois 60208, United States;* orcid.org/0000-0003-2248-474X

Complete contact information is available at: https://pubs.acs.org/10.1021/acs.chemmater.2c00223

Author Contributions

‖C.C.L. and J.S. contributed equally to this work.

Notes

The authors declare no competing financial interest.

■ ACKNOWLEDGMENTS

Synthesis and material characterization were supported by the National Science Foundation through Grant DMR-2003476. J.S. acknowledges the support from the MRSEC program (DMR-1720319) at the Materials Research Center of Northwestern University. This work used the IMSERC Crystallography facility at Northwestern University, which received support from the Soft and Hybrid Nanotechnology Experimental (SHyNE) Resource (NSF ECCS-2025633) and Northwestern University. The Ag-microsource diffractometer used in this study was funded by the Major Research Instrumentation Program from the National Science Foundation under the award CHE-1920248. C.C.L. acknowledges Christos D. Malliakas for assistance in setting up the low-temperature single crystal collection. This work used the IMSERC Physical Characterization facility at Northwestern University, which has received support from the SHyNE Resource (NSF ECCS-2025633), and Northwestern University. This work used the EPIC facility of Northwestern University's NUANCE Center, which received support from the SHyNE Resource (NSF ECCS-2025633), IIN, and Northwestern University's MRSEC program (NSF DMR-1720139). Computational resources were provided by the National Energy Research Scientific Computing Center (NERSC), U.S. Department of Energy Office of Science User Facility, operated under Contract No. DE-AC02-05CH11231, and the Quest High Performance Computing facility at Northwestern University.

■ REFERENCES

(1) Huang, F. Q.; Ibers, J. A. Syntheses and Structures of the Quaternary Copper Tellurides $K_3Ln_4Cu_5Te_{10}$ (Ln = Sm, Gd, Er), $Rb_3Ln_4Cu_5Te_{10}$ (Ln = Nd, Gd), and $Cs_3Gd_4Cu_5Te_{10}$. *J. Solid State Chem.* **2001**, *160* (2), 409−414.

(2) Lissner, F.; Meyer, S. P.; Schleid, T. $CsTb_3STe_4$ und $CsTb_5S_2Te_6$: two pseudo-ternary cesium terbium chalcogenides with ordered S^{2-} and Te^{2-} anions. *Zeitschrift für Naturforschung B* **2019**, *74* (1), 99−107.

(3) Patschke, R.; Brazis, P.; Kannewurf, C. R.; Kanatzidis, M. $K_2Ag_3CeTe_4$: A Semiconducting Tunnel Framework Made from the Covalent "Link-Up" of $[Ag_2CeTe_4]^{3-}$ Layers with Ag. *Inorg. Chem.* **1998**, *37* (26), 6562−6563.

(4) Huang, F. Q.; Mitchell, K.; Ibers, J. A. New Layered Materials: Syntheses, Structures, and Optical and Magnetic Properties of $CsGdZnSe_3$, $CsZrCuSe_3$, $CsUCuSe_3$, and $BaGdCuSe_3$. *Inorg. Chem.* **2001**, *40* (20), 5123−5126.

(5) Eickmeier, K.; Steinberg, S. Revealing the Bonding Nature in an $ALnZnTe_3$ -Type Alkaline-Metal (A) Lanthanide (Ln) Zinc Telluride by Means of Experimental and Quantum-Chemical Techniques. *Crystals* **2020**, *10* (10), 916.
(6) Usman, M.; Smith, M. D.; Morrison, G.; Klepov, V. V.; Zhang, W.; Halasyamani, P. S.; zur Loye, H.-C. Molten Alkali Halide Flux Growth of an Extensive Family of Noncentrosymmetric Rare Earth Sulfides: Structure and Magnetic and Optical (SHG) Properties. *Inorg. Chem.* **2019**, *58* (13), 8541−8550.
(7) Patschke, R.; Brazis, P.; Kannewurf, C. R.; Kanatzidis, M. G. $Cu_{0.66}EuTe_2$, KCu_2EuTe_4 and $Na_{0.2}Ag_{2.8}EuTe_4$: compounds with modulated square Te nets. *J. Mater. Chem.* **1999**, *9* (10), 2293−2296.
(8) Patschke, R.; Kanatzidis, M. G. Polytelluride compounds containing distorted nets of tellurium. *Phys. Chem. Chem. Phys.* **2002**, *4* (14), 3266−3281.
(9) Mitchell, K.; Ibers, J. A. Rare-Earth Transition-Metal Chalcogenides. *Chem. Rev.* **2002**, *102* (6), 1929−1952.
(10) Eberle, M. A.; Schleid, T. Two Isotypic Alkali-Metal Copper Yttrium Sulfides: $KCuY_2S_4$ and $RbCuY_2S_4$. *Zeitschrift für anorganische und allgemeine Chemie* **2012**, *638* (10), 1593−1593.
(11) Babo, J.-M.; Strobel, S.; Schleid, T. Syntheses and Crystal Structures of $CsCuNd_2Se_4$ and $CsCuGd_2Te_4$: Two Non-Isotypical Cesium Copper Lanthanide Chalcogenides with $\{[CuCh_3]^{5-}\}$ Chains of Vertex-Shared $[CuCh_4]^{7-}$ Tetrahedra. *Zeitschrift für anorganische und allgemeine Chemie* **2010**, *636* (2), 349−355.
(12) Stoll, P.; Dürichen, P.; Näther, C.; Bensch, W. Synthesis and Crystal Structure of $KCuGd_2S_4$: A Threedimensional Framework with Isolated Channels. *Zeitschrift für anorganische und allgemeine Chemie* **1998**, *624* (11), 1807−1810.
(13) Yao, J.; Deng, B.; Ellis, D. E.; Ibers, J. A. Syntheses, structures, physical properties, and electronic structures of KLn_2CuS_4 (Ln = Y, Nd, Sm, Tb, Ho) and $K_2Ln_4Cu_4S_9$ (Ln = Dy, Ho). *J. Solid State Chem.* **2003**, *176* (1), 5−12.
(14) Feudjio, J. P. J. Ternary Rare-Earth Coinage Metal Arsenides $LnTAs_2$, $Sm_2Cu_3As_3$; Quaternary Arsenide Oxides Sm_2CuAs_3O and Selenides KGd_2CuSe_4, $KLn_2Cu_3Se_5$, and $K_2Ln_4Cu_4Se_9$ (Ln= Y, La-Nd, Sm, Gd-Lu; T= Cu, Ag, Au): Syntheses, Crystal Structures and Physical Properties. Dissertation, University of Technology, Dresden, 2004.
(15) Huang, F. Q.; Ibers, J. A. Syntheses, Structures, and Physical Properties of the New Quaternary Rare-Earth Chalcogenides $RbNd_2CuS_4$, $RbSm_2CuS_4$, $CsLa_2CuSe_4$, $CsSm_2CuSe_4$, $RbEr_2Cu_3S_5$, $CsGd_2Ag_3Se_5$, $CsTb_2Ag_3Se_5$, and $Rb_2Gd_4Cu_4S_9$. *J. Solid State Chem.* **2001**, *158* (2), 299−306.
(16) Huang, F. Q.; Ibers, J. A. Syntheses and Structures of the New Quaternary Rubidium Selenides $RbLn_2CuSe_4$ (Ln = Sm, Gd, Dy), $Rb_{1.5}Ln_2Cu_{2.5}Se_5$ (Ln = Gd, Dy), and $RbSm_2Ag_3Se_5$. *J. Solid State Chem.* **2000**, *151* (2), 317−322.
(17) Yao, J.; Ibers, J. A. $RbGd_2CuS_4$. *Acta Crystallographica Section E* **2004**, *60* (8), i95−i96.
(18) Zeng, H.-Y.; Mao, J.-G.; Chen, J.-T.; Dong, Z.-C.; Guo, G.-C.; Huang, J.-S. Synthesis and structure of IR-transparent rare-earth selenides KLn_2CuSe_4 (Ln = Ho, Er). *J. Alloys Compd.* **2002**, *336* (1), 148−153.
(19) Lauxmann, P.; Schleid, T. $CsCu_3Dy_2S_5$ and $CsCu_3Er_2S_5$: Two Isotypic Quaternary Sulfides of the Lanthanides with Channel Structures. *Zeitschrift für Naturforschung B* **2001**, *56* (11), 1149−1154.
(20) Zeng, H.-Y.; Mao, J.-G.; Zhenchao, D.; Guo, G.-C.; Huang, J.-S. Synthesis annd single crystal structure of $RbEr_2Cu_3Se_5$. *Jiegou Huaxue* **2002**, *21* (5), 497−500.
(21) Strobel, S.; Schleid, T. Quaternary Cesium Copper(I) Lanthanoid(III) Selenides of the Type $CsCu_3M_2Se_5$(M = Sm, Gd - Lu). *Zeitschrift für anorganische und allgemeine Chemie* **2004**, *630* (5), 706−711.
(22) Yao, J.; Ibers, J. A. $RbHo_2Cu_3S_5$. *Acta Crystallographica Section E* **2004**, *60* (9), i118−i119.
(23) Kanatzidis, M. G. Structural Evolution and Phase Homologies for "Design" and Prediction of Solid-State Compounds. *Acc. Chem. Res.* **2005**, *38* (4), 359−368.
(24) McCarthy, T. J.; Ngeyi, S. P.; Liao, J. H.; DeGroot, D. C.; Hogan, T.; Kannewurf, C. R.; Kanatzidis, M. G. Molten salt synthesis and properties of three new solid-state ternary bismuth chalcogenides, β-$CsBiS_2$, γ-$CsBiS_2$, and $K_2Bi_8Se_{13}$. *Chem. Mater.* **1993**, *5* (3), 331−340.
(25) Liao, J. H.; Varotsis, C.; Kanatzidis, M. G. Syntheses, structures, and properties of six novel alkali metal tin sulfides: $K_2Sn_2S_8$, α-$Rb_2Sn_2S_8$, β-$Rb_2Sn_2S_8$, $K_2Sn_2S_5$, $Cs_2Sn_2S_6$, and Cs_2SnS_{14}. *Inorg. Chem.* **1993**, *32* (11), 2453−2462.
(26) Baláž, M.; Zorkovská, A.; Urakaev, F.; Baláž, P.; Briančin, J.; Bujňáková, Z.; Achimovičová, M.; Gock, E. Ultrafast mechanochemical synthesis of copper sulfides. *RSC Adv.* **2016**, *6* (91), 87836−87842.
(27) STOE & Cie. *X-area*, version 1.90; *X-red*, version 1.65.2; *X-Shape*, version 2.21; *STOE LANA*, version 1.83.8; 2020.
(28) Sheldrick, G. SHELXT - Integrated space-group and crystal-structure determination. *Acta Crystallogr., Sect. A* **2015**, *71* (1), 3−8.
(29) Sheldrick, G. Crystal structure refinement with SHELXL. *Acta Crystallographica Section C* **2015**, *71* (1), 3−8.
(30) Dolomanov, O. V.; Bourhis, L. J.; Gildea, R. J.; Howard, J. A. K.; Puschmann, H. OLEX2: a complete structure solution, refinement and analysis program. *J. Appl. Crystallogr.* **2009**, *42* (2), 339−341.
(31) Hohenberg, P.; Kohn, W. Inhomogeneous Electron Gas. *Phys. Rev.* **1964**, *136* (3B), B864−B871.
(32) Kohn, W.; Sham, L. J. Self-Consistent Equations Including Exchange and Correlation Effects. *Phys. Rev.* **1965**, *140* (4A), A1133−A1138.
(33) Kresse, G.; Furthmüller, J. Efficiency of ab-initio total energy calculations for metals and semiconductors using a plane-wave basis set. *Comput. Mater. Sci.* **1996**, *6* (1), 15−50.
(34) Kresse, G.; Furthmüller, J. Efficient iterative schemes for ab initio total-energy calculations using a plane-wave basis set. *Phys. Rev. B* **1996**, *54* (16), 11169−11186.
(35) Blöchl, P. E. Projector augmented-wave method. *Phys. Rev. B* **1994**, *50* (24), 17953−17979.
(36) Perdew, J. P.; Burke, K.; Ernzerhof, M. Generalized Gradient Approximation Made Simple. *Phys. Rev. Lett.* **1996**, *77* (18), 3865−3868.
(37) Kresse, G.; Joubert, D. From ultrasoft pseudopotentials to the projector augmented-wave method. *Phys. Rev. B* **1999**, *59* (3), 1758−1775.
(38) Saal, J. E.; Kirklin, S.; Aykol, M.; Meredig, B.; Wolverton, C. Materials Design and Discovery with High-Throughput Density Functional Theory: The Open Quantum Materials Database (OQMD). *JOM* **2013**, *65* (11), 1501−1509.
(39) Kirklin, S.; Saal, J. E.; Meredig, B.; Thompson, A.; Doak, J. W.; Aykol, M.; Rühl, S.; Wolverton, C. The Open Quantum Materials Database (OQMD): assessing the accuracy of DFT formation energies. *npj Computational Materials* **2015**, *1* (1), 15010.
(40) Togo, A.; Tanaka, I. First principles phonon calculations in materials science. *Scripta Materialia* **2015**, *108*, 1−5.
(41) Xia, Y.; Pal, K.; He, J.; Ozoliņš, V.; Wolverton, C. Particlelike Phonon Propagation Dominates Ultralow Lattice Thermal Conductivity in Crystalline Tl_3VSe_4. *Phys. Rev. Lett.* **2020**, *124* (6), 065901.
(42) Zhou, F.; Nielson, W.; Xia, Y.; Ozoliņš, V. Lattice Anharmonicity and Thermal Conductivity from Compressive Sensing of First-Principles Calculations. *Phys. Rev. Lett.* **2014**, *113* (18), 185501.
(43) Zhou, F.; Nielson, W.; Xia, Y.; Ozoliņš, V. Compressive sensing lattice dynamics. I. General formalism. *Phys. Rev. B* **2019**, *100* (18), 184308.
(44) Zhou, F.; Sadigh, B.; Åberg, D.; Xia, Y.; Ozoliņš, V. Compressive sensing lattice dynamics. II. Efficient phonon calculations and long-range interactions. *Phys. Rev. B* **2019**, *100* (18), 184309.
(45) Li, W.; Carrete, J.; Katcho, N. A.; Mingo, N. ShengBTE: A solver of the Boltzmann transport equation for phonons. *Comput. Phys. Commun.* **2014**, *185* (6), 1747−1758.

(46) Madsen, G. K. H.; Singh, D. J. BoltzTraP. A code for calculating band-structure dependent quantities. *Comput. Phys. Commun.* **2006**, *175* (1), 67−71.
(47) Grimvall, G. *The Electron-Phonon Interaction in Metals*; North-Holland: Amsterdam, 1981.
(48) Ganose, A. M.; Park, J.; Faghaninia, A.; Woods-Robinson, R.; Persson, K. A.; Jain, A. Efficient calculation of carrier scattering rates from first principles. *Nat. Commun.* **2021**, *12* (1), 2222.
(49) Deng, B.; Yao, J.; Ibers, J. A. Dicerium orthosilicate selenide and dicerium orthosilicate telluride, $Ce_2(SiO_4)Q$ (Q = Se or Te). *Acta Crystallographica Section C* **2004**, *60* (11), i110−i112.
(50) Babo, J.-M.; Choi, E. S.; Albrecht-Schmitt, T. E. Synthesis, Structure, Magnetism, and Optical Properties of $Cs_2Cu_3DyTe_4$. *Inorg. Chem.* **2012**, *51* (21), 11730−11735.
(51) Babo, J.-M.; Schleid, T. $CsCu_2Sc_3Te_6$ and $CsCuY_2Te_4$: Two new quaternary cesium copper rare-earth metal tellurides. *Solid State Sci.* **2010**, *12* (2), 238−245.
(52) Kortüm, G.; Braun, W.; Herzog, G. Principles and Techniques of Diffuse-Reflectance Spectroscopy. *Angewandte Chemie International Edition in English* **1963**, *2* (7), 333−341.

https://doi.org/10.1021/acs.chemmater.2c00223
Chem. Mater. 2022, 34, 3409−3422